




ARTICLE

DOI: 10.1038/s41467-018-04547-4

OPEN

Quantum Monte Carlo simulations of a giant $\{\text{Ni}_{21}\text{Gd}_{20}\}$ cage with a $S = 91$ spin ground state

Wei-Peng Chen¹, Jared Singleton², Lei Qin¹, Agustín Camón³,
Larry Engelhardt², Fernando Luis ³, Richard E.P. Winpenny ⁴ & Yan-Zhen Zheng ¹

The detailed analysis of magnetic interactions in a giant molecule is difficult both because the synthesis of such compounds is challenging and the number of energy levels increases exponentially with the magnitude and number of spins. Here, we isolated a $\{\text{Ni}_{21}\text{Gd}_{20}\}$ nanocage with a large number of energy levels ($\approx 5 \times 10^{30}$) and used quantum Monte Carlo (QMC) simulations to perform a detailed analysis of magnetic interactions. Based on magnetization measurements above 2 K, the QMC simulations predicted very weak ferromagnetic interactions that would give a record $S = 91$ spin ground state. Low-temperature measurements confirm the spin ground state but suggest a more complex picture due to the single ion anisotropy; this has also been modeled using the QMC approach. The high spin and large number of low-lying states lead to a large low-field magnetic entropy ($14.1 \text{ J kg}^{-1} \text{ K}^{-1}$ for $\Delta H = 1 \text{ T}$ at 1.1 K) for this material.

¹Frontier Institute of Science and Technology (FIST), State Key Laboratory for Mechanical Behavior of Materials, MOE Key Laboratory for Nonequilibrium Synthesis and Modulation of Condensed Matter, and School of Science, Xi'an Jiaotong University, 99 Yanxiang Road, Xi'an, Shaanxi 710054, China.

²Department of Physics and Astronomy, Francis Marion University, Florence, SC 29502, USA. ³Instituto de Ciencia de Materiales de Aragón (ICMA) and Departamento de Física de la Materia Condensada, CSIC-Universidad de Zaragoza, E-50009 Zaragoza, Spain. ⁴Department of Chemistry and Photon Science Institute, The University of Manchester, Manchester M13 9PL, UK. Correspondence and requests for materials should be addressed to L.E. (email: lengelhardt@fmarion.edu) or to R.E.P.W. (email: richard.winpenny@manchester.ac.uk) or to Y.-Z.Z. (email: zheng.yanzhen@xjtu.edu.cn)

Paramagnetic metal clusters possessing large ground spin state (S) often show attractive magnetic behavior with potential applications such as single-molecule magnets (SMMs)^{1,2}, magnetic refrigerants^{3,4}, and contrast agents for magnetic resonance imaging (MRI)^{5,6}. To date, the highest ground spin states reported are $S = 83/2$ for a $\{\text{Mn}_{19}\}$ cage⁷, $S = 61/2$ for a $\{\text{Mn}_{49}\}$ cage², $S = 45$ for an $\{\text{Fe}_{42}\}$ cage⁸, and $S = 60$ for a $\{\text{Fe}_{10}\text{Gd}_{10}\}$ nano-torus⁹. The accurate magnetic analysis of such giant species is challenging because the number of energy levels increases exponentially with the magnitude and number of spins. For example, the famous SMM, $\{\text{Mn}_{12}\}$ requires a diagonalization of a matrix with the dimension of 10^8 and this has only recently been achieved^{10–12}. Quantum Monte Carlo (QMC) simulation may provide a useful alternative for the investigation of large systems¹³. Successful examples include both ring^{14–17} and cage¹⁸ structures. A further level of complexity can arise if significant single-ion anisotropy is present as this can compete with exchange interactions in deciding low-temperature physics.

Application of molecules with very high spin as magnetic refrigerants^{19–21}, requires molecules with a large spin ground state, weak ferromagnetic exchange, and negligible magnetic anisotropy^{3,4}. Cages based on gadolinium ions are excellent candidates to achieve such goals^{22–24} if ferromagnetic exchange can be induced. Controlling the sign of magnetic exchange is difficult, but we noticed two cases where ferromagnetic exchange is normally observed. Firstly, the *syn-anti* bridging mode in nickel(II) carboxylate complexes usually causes ferromagnetic exchange between nickel(II) ions²⁵. Secondly, where two gadolinium(III) ions are bridged by a single O-atom, a large Gd–O–Gd angle ($>110.9^\circ$) yields ferromagnetic exchange between Gd ions²⁶. The $\{\text{Ni}_{21}\text{Ln}_{20}\}$ cages ($\text{Ln} = \text{Pr}$ and Nd) reported by Kong et al.²⁷ contain the correct bridging mode for the Ni(II) units, and the Ln–O–Ln angles are large. However, this group was unable to produce the Gd analog, and the yields reported of other $\{\text{Ni}_{21}\text{Ln}_{20}\}$ clusters were low. These compounds feature 2-hydroxyl-acetate as a ligand, and this is formed in situ from the

decomposition of iminodiacetic acid (IDA_2), which was the ligand added to the reaction. This in situ formation of a key ingredient probably explains the low yields.

Therefore we carried out similar chemistry, but included diphenylglycolic acid (DPGA_2), which has the same donor groups as 2-hydroxyl-acetate. This produces the spherical cage complex $[\text{Ni}_{21}\text{Gd}_{20}(\text{OH})_{24}(\text{IDA})_{21}(\text{DPGA})_6(\text{C}_2\text{O}_4)_3(\text{NO}_3)_6(\text{CH}_3\text{COO})_3(\text{H}_2\text{O})_{12}]\cdot\text{Br}_5\cdot(\text{NO}_3)_4\cdot 20\text{CH}_3\text{OH}\cdot 30\text{H}_2\text{O}$ (**1**) in good yield. QMC simulations were carried out to analyze the magnetic exchange in this nanocage $\{\text{Ni}_{21}\text{Gd}_{20}\}$. The magnetic metal centres are ferromagnetically coupled, approaching a $S = 91$ spin ground state, but single-ion anisotropy competes with the exchange interactions, leading to a more complex magnetic state with large low field entropy ($14.1 \text{ J kg}^{-1} \text{ K}^{-1}$ for $\Delta H = 1 \text{ T}$ at 1.1 K), which is a new record in cryogenic cluster-based magnetic refrigerants to the best of our knowledge^{19–21}.

Results

Structure of $\{\text{Ni}_{21}\text{Gd}_{20}\}$ cage. Single-crystal X-ray diffraction analyses reveal that **1** crystallizes in the hexagonal space group $P6_3/m$ (Supplementary Table 1). The spherical structure of the cationic cluster may be viewed as constructed from an inner $\{\text{Gd}_{20}\}$ core and the outer $\{\text{Ni}_{21}\}$ shell (Fig. 1a and Supplementary Fig. 1). The inner $\{\text{Gd}_{20}\}$ core contains two bowl-like Gd_{10} subunits made up of a triangle of three pentagonal $\text{Gd}_5(\text{NO}_3)_3$ fragments that share four Gd(III) ions (Supplementary Fig. 1). The NO_3^- ions sit in the middle of the pentagonal $\text{Gd}_5(\text{NO}_3)_3$ fragments with a 5.222 bridging mode (Harris notation). Three $\mu\text{-OH}^-$, three $\mu\text{-acetate}$ bridges and three $\text{C}_2\text{O}_4^{2-}$ ligands link the two bowl-like Gd_{10} subunits to form the $\{\text{Gd}_{20}\}$ core. The Gd–O distances ($2.29\text{--}2.72 \text{ \AA}$) and the Gd(III)⋯Gd(III) separations ($3.89\text{--}4.18 \text{ \AA}$) in this core are comparable to other reported Gd-based clusters. Note that the Gd–O–Gd angles ranging from 104.7° to 120.3° average at 111.0° (Supplementary Table 2), which usually causes ferromagnetic exchange between Gd(III) ions²⁶.

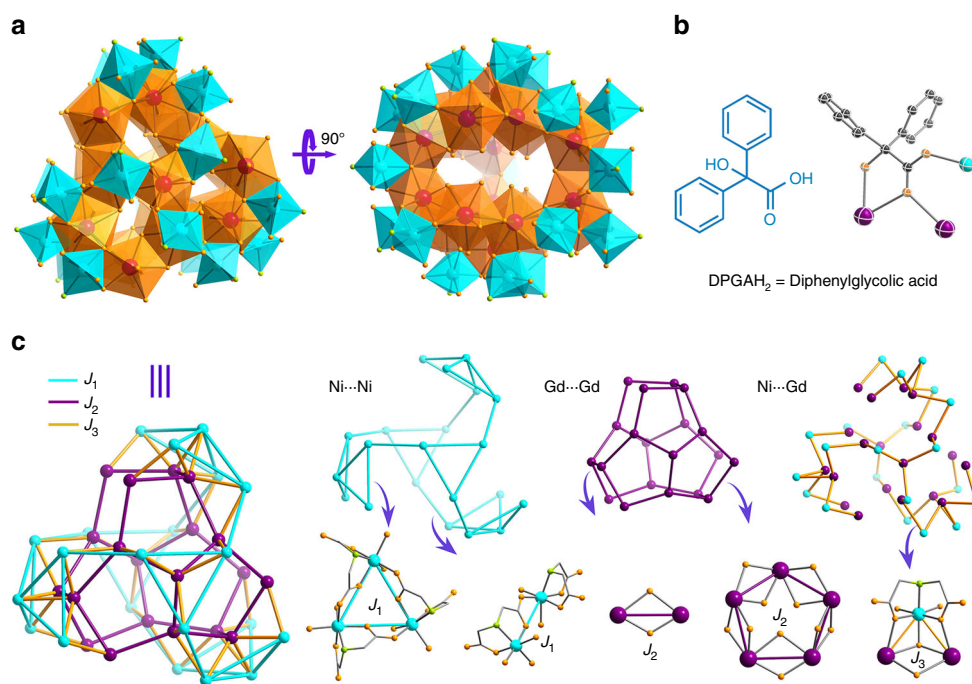


Fig. 1 The structure of nanocage $\{\text{Ni}_{21}\text{Gd}_{20}\}$ determined by X-ray crystallography. **a** The polyhedron structures of $\{\text{Ni}_{21}\text{Gd}_{20}\}$ core with the organic ligands removed for clarity; **b** The coordination mode of the DPGA_2^- ligand in this compound; **c** The magnetic coupling schemes of the metal centers in $\{\text{Ni}_{21}\text{Gd}_{20}\}$ core. $J_1 = \text{Ni}\cdots\text{Ni}$, $J_2 = \text{Gd}\cdots\text{Gd}$, $J_3 = \text{Ni}\cdots\text{Gd}$; Color codes: Gd purple, Ni cyan, N green, O orange, C gray

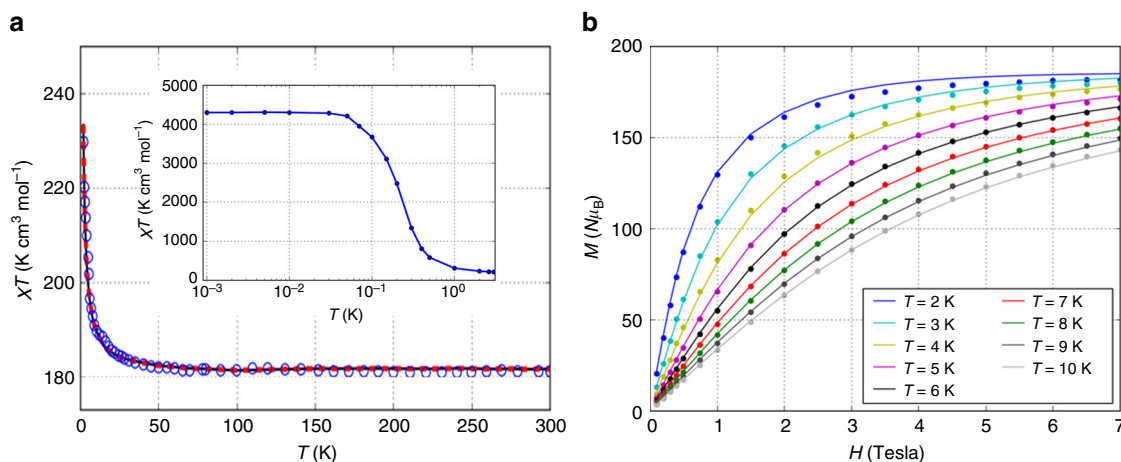


Fig. 2 The magnetic characteristics for compound **1**. **a** The temperature dependences of χT versus T . The experimental data are shown as circles, and the solid curve is for the single J -model, assuming $D_{\text{Ni}} = 0$ with $J/k_{\text{B}} = -0.033$ K (best fit). **b** Magnetization versus field for several fixed values of temperature using the single J -model (with $D_{\text{Ni}} = 0$) that provides the best fit to the susceptibility. The experimental data are shown as dots and theory data shown as solid curve. (Inset of **a**) Low-temperature predictions of the isotropic Heisenberg model for χT versus T

The inner $\{\text{Gd}_{20}\}$ core and outer $\{\text{Ni}_{21}\}$ shell are connected by six DPGA^{2-} ligands, 24 μ_3 -hydroxides and twenty-one O atoms of IDA^{2-} to form a spherical framework $\{\text{Ni}_{21}\text{Gd}_{20}\}$ with the Ni (II)–Gd(III) distances ranging from 3.46 to 3.63 Å. In the external $\{\text{Ni}_{21}\}$ shell (Supplementary Fig. 1), there are three $\{\text{Ni}(\text{IDA})\}_5$ fragments and two $\{\text{Ni}(\text{IDA})\}_3$ units, which are bound to carboxylate groups from IDA ligands. The butterfly-shaped $\{\text{Ni}(\text{IDA})\}_5$ fragments are located in the equatorial zones of the sphere, while two $\{\text{Ni}(\text{IDA})\}_3$ units sit at the two poles. The IDA ligands adopt the *syn-anti* bridging mode to connect adjacent Ni (II) ions to form the $\{\text{Ni}(\text{IDA})\}_{21}$ shell. The Ni–O bond distances, Ni–N bond distances and Ni(II)–Ni(II) separations range from 1.99 to 2.10, 2.08 to 2.11, and 5.16 to 5.28 Å (Supplementary Table 2), respectively.

Magnetic properties. The magnetic behavior of a polycrystalline powder sample of **1** was studied in the temperature range $T = 2$ –300 K under a 1000 Oe dc field, as shown in Fig. 2a. The χT value of $181.3 \text{ K cm}^3 \text{ mol}^{-1}$ at room temperature is only slightly below the high-temperature Curie limit of $182.9 \text{ K cm}^3 \text{ mol}^{-1}$ that would be expected for 21 uncorrelated Ni(II) ions ($S = 1$, $g = 2.2$) and 20 uncorrelated Gd(III) ions ($S = 7/2$, $g = 2$). Upon cooling, χT remains relatively constant until 35 K and then increases abruptly, reaching a value of $229.8 \text{ K cm}^3 \text{ mol}^{-1}$ at 2 K without saturation (Fig. 2a). This rapid rise of χT suggests that predominantly ferromagnetic interactions are present. This is supported by fitting the inverse molar susceptibility between $T = 100$ and 300 K using the Curie–Weiss equation, which gives $C = 180.8 \text{ K cm}^3 \text{ mol}^{-1}$ and $\theta = 0.36$ K (Supplementary Fig. 2).

The field-dependent molar magnetization, $M(H)$, of **1** was also measured for the temperature range $T = 2$ –10 K in the field range $H = 0$ –7 T (Fig. 2b). Fig. 2b shows that for $T = 2.0$ K, $M(H)$ rapidly increases for $H < 1$ T, and then begins to flatten out for $H > 2$ T, nearly saturating and reaching a value of $M = 181.7 N\mu_{\text{B}}$ (where N is the Avogadro constant and μ_{B} is the Bohr magneton). This value is very close to the expected high-field limit of $M = 182 N\mu_{\text{B}}$ for $g = 2.0$ and $S = 91$. The measured magnetization curves are slightly higher than the corresponding Brillouin curves corresponding to 41 non-interacting spins, and very substantially lower than the Brillouin curve for $S = 91$ ground spin state (Supplementary Fig. 3). This is again consistent with weak ferromagnetic coupling within the molecule.

The detailed investigation of inter-ion exchange coupling in giant 3d–4f polymetallic complex systems has always been a challenge due to the large number of magnetic states. Since **1** consists of 20 Gd(III) ions with $S = 7/2$ and 21 Ni(II) ions with $S = 1$, the number of the states is $\approx 5 \times 10^{30}$, so matrix diagonalization is not possible. Instead, we calculated χT using a QMC method with the stochastic series expansion implementation from Algorithms and Libraries for Physics Simulations (ALPS), as shown in Fig. 2 (solid curves)^{28,29,30}. For these simulations, we assumed a Hamiltonian of the form

$$\hat{H} = J_1 \sum_{\text{Ni}, \text{Ni}} \hat{s}_i \cdot \hat{s}_j + J_2 \sum_{\text{Gd}, \text{Gd}} \hat{s}_i \cdot \hat{s}_j + J_3 \sum_{\text{Ni}, \text{Gd}} \hat{s}_i \cdot \hat{s}_j + D_{\text{Ni}} \sum_{\text{Ni}} \hat{s}_{jz}^2 - \mu_{\text{B}} H \sum_i g_i \hat{s}_{iz}$$

which uses the sign convention where $J < 0$ represents a ferromagnetic interaction and omitting the single ion magnetic anisotropy on the Gd(III) sites.

The Ni(II)–Ni(II), Gd(III)–Gd(III), and Ni(II)–Gd(III) distances in this cluster range from 5.16 to 5.28, 3.89 to 4.18, and 3.46 to 3.63 Å, respectively; so three exchange interactions were used to describe the system: J_1 corresponds to the Ni–Ni interactions, J_2 to Gd–Gd, and J_3 to Ni–Gd (Fig. 1c). In order to reduce the size of the parameter space to be explored, we initially set $D_{\text{Ni}} = 0$, which corresponds to a purely isotropic Heisenberg Hamiltonian with three exchange constants. The values $g_{\text{Gd}} = 1.99$ and $g_{\text{Ni}} = 2.196$ were determined from the measured susceptibility, especially the high-temperature data.

Using the isotropic Heisenberg Hamiltonian described above, we were able to get a very good fit to the measured data in the range $T = 2$ –300 K, as shown in Fig. 2. When allowing all three exchange interactions to vary, the parameter values that gave the best fit were: $J_1/k_{\text{B}} = -0.0305$ K, $J_2/k_{\text{B}} = -0.0302$ K, and $J_3/k_{\text{B}} = -0.0516$ K (all ferromagnetic interactions). Since these three J values are very similar, we considered a single- J model, constraining all three J values to be equal to each other. For the single- J model, we found $J/k_{\text{B}} = -0.033$ K, and the goodness of fit for the single J value was virtually identical to the goodness of fit

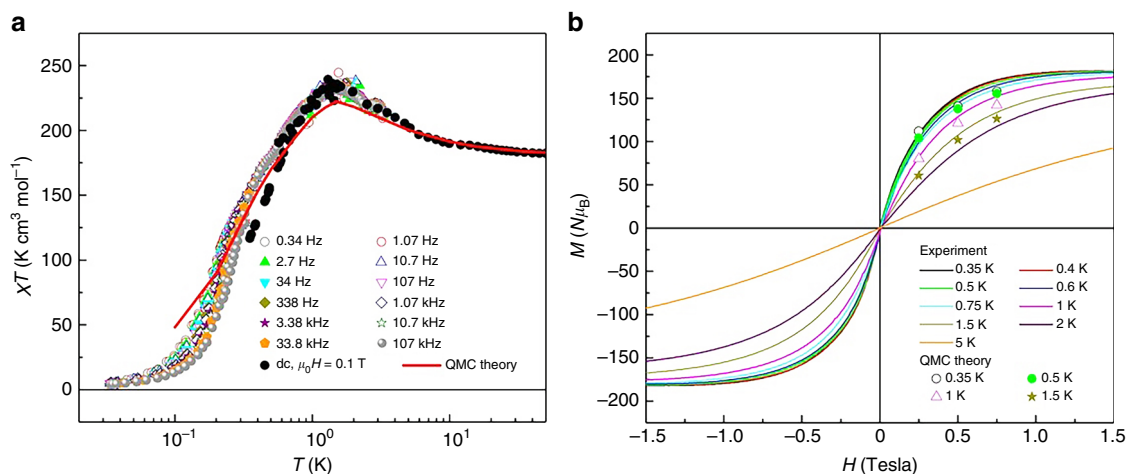


Fig. 3 Very low-temperature magnetic behavior. **a** Temperature dependence of χT measured at $H = 0$ and in the region of very low temperatures for different frequencies. Dc data measured under a magnetic field $H = 0.1$ T are also shown. Experimental data are represented with symbols, and the solid line represents the best-fit for the anisotropic model described in the text. **b** Magnetization versus field isotherms measured at very low temperatures. Solid curves: measured magnetizations at temperatures given. Symbols: QMC calculated magnetizations using the best-fit parameters given in the text

Table 1 ΔS_M at low-field (<2 T) for reported polymetallic molecules

Complexes	$-\Delta S_M$ (J kg ⁻¹ K ⁻¹)	$-\Delta S_M$ (J kg ⁻¹ K ⁻¹)	$-\Delta S_M$ (J kg ⁻¹ K ⁻¹)	T (K)	Ref
	2.0 T	1.0 T	0.5 T		
{Gd ^{III} ₂₄ }	22.6	10	6	2.0	32
{Ni ^{II} ₂₁ Gd ^{III} ₂₀ } (1)	19.8	14.1	6.6	2.0/1.1	This work
{Ni ^{II} ₆₄ Gd ^{III} ₉₆ }	17	7.0	2.0	3.0	22
{Gd ^{III} ₁₀ }	17	8.0	3.5	2.0	33
{Co ^{II} ₄ Gd ^{III} ₁₀ }	15	3.7	2.3	3.0	34
{Co ^{II} ₉ Co ^{III} Gd ^{III} ₄₂ }	14	5.0	2.0	2.0	35
{Gd ₁₂ Mo ₄ }	14	5.0	1.8	3.0	36
{Gd ^{III} ₄₈ }	13.7	5.0	2.0	1.8	37
{Ni ^{II} ₁₀ Gd ^{III} ₄₂ }	13.5	4.8	2.0	2.0	35
{Mn ^{II} ₄ Gd ^{III} ₆ }	13.5	5.0	1.5	2.0	38

for the three- J model. (See Supplementary Figs. 4 and 5 for details regarding the goodness of fit.)

The ferromagnetic exchange interactions described above predict a $S = 91$ spin ground state with $\chi T \approx 4300$ K cm³ mol⁻¹ at very low temperatures, as shown in the inset of Fig. 2a. However, this spin ground state is not isolated, and to this point we have neglected any single-ion anisotropy by setting $D_{Ni} = 0$, which could be important for Ni(II). It is perhaps surprising that an isotropic model, which we have used to this point, models the 2–300 K data so well.

To establish whether or not this prediction of a record $S = 91$ spin ground state is correct, we carried out lower temperature magnetic measurements (supplementary Fig. 6). These results show that the picture of an isotropic $S = 91$ spin ground state is simplistic. The zero-field ac susceptibility (supplementary Figs. 7 and 8) departs, below 2 K, from the paramagnetic behavior observed at higher temperatures. The χT product (Fig. 3a) reaches a maximum at about 1.5 K and then decreases. Also, χ becomes frequency-dependent below 350 mK, which shows the existence of slow magnetic relaxation processes. The characteristic spin-lattice relaxation time increases with decreasing T and becomes of the order of seconds near 0.1 K (supplementary Fig. 9). This slow magnetic relaxation can be associated with a zero-field splitting

that originates from the finite magnetic anisotropy of the constituent Gd(III) or Ni(II) ions. The activation energy $U/k_B = 3.3$ K that governs these processes is close to values found for Gd-based single-ion magnets³¹.

To model these new data, we expanded our QMC approach to include an axial zero-field splitting for the Ni(II) ions, $D_{Ni} \neq 0$. We initially used the single J -model with $D_{Ni} \neq 0$, which gave two free parameters, J and D_{Ni} ; but within this two-dimensional parameter space it was not possible to produce a peak in χT around $T = 1.5$ K. Thus we expanded our search to the full four-dimensional parameter space of the Hamiltonian (J_1, J_2, J_3, D_{Ni}). There is now a danger of over-parameterization, however a key feature of the QMC approach is that we are able to examine a massive segment of parameter space, and hence the possibility of false minima is reduced. In this expanded parameter space, we were indeed able to get a reasonably good fit to the measured χT curve, as shown in Fig. 3a. The set of parameters that gives this best fit is: $J_1/k_B = -0.0225$ K, $J_2/k_B = -0.0113$ K, and $J_3/k_B = -0.225$ K (all ferromagnetic) and $D_{Ni}/k_B = 2.5$ K (hard axis anisotropy), where—although these J values are listed using three digits—we estimate that a range of about $\pm 10\%$ around each parameter value will still give a similarly good fit. This model was also used to compute the M versus H data shown as filled circles in Fig. 3b. For each of these low temperatures, we find that this model gives magnetization values that are slightly higher than the measured values; but for $T \geq 2$ K, this anisotropic model actually agrees with the measured magnetization slightly better than the isotropic model. (See Supplementary Fig. 10, as compared with Fig. 2.)

The magnetic entropy changes ΔS_m were evaluated by applying the Maxwell relation $-\Delta S_m(T) = \int [\partial M(T, H) / \partial T]_H dH$ on the cluster **1**. Calculated entropy changes obtained from magnetization and heat capacity (Supplementary Fig. 11) data give a maximum value of 34.8 J kg⁻¹ K⁻¹ at 3 K and 7 T for **1** (Supplementary Fig. 12), which is comparable to other Gd-based polymetallic clusters (Supplementary Table 3)², but smaller than the maximum entropy value judged by the function of $-\Delta S_m = nR \ln(2S + 1) = 64.7 R$, which corresponds to 45.8 J kg⁻¹ K⁻¹ for **1**. The coupling between the Gd(III) and Ni(II) ions, as well as their finite magnetic anisotropies, reduce the maximum achievable entropy content because these interactions partly lift the level degeneracy at $H = 0$. However, the dominant ferromagnetic couplings also enable reaching sizeable $-\Delta S_m$ values at moderate

magnetic fields. A large low-field magnetic entropy change, reaching $14.1 \text{ J kg}^{-1} \text{ K}^{-1}$ for a magnetic field change of 1 T at 1.1 K, is observed (Table 1).

Discussion

The analysis of the magnetic properties of giant heterometallic paramagnetic molecules, such as the one presented here, is rare due to the multiple magnetic couplings and the large number of magnetic states. In **1**, there are three different inter-ion exchange interactions and 99 connections (30 J_1 , 27 J_2 and 42 J_3 , see Fig. 1c), and the number of the states reaches 5×10^{30} even before we allow for any anisotropy. Thus the simulation of the magnetic interaction in such a large system through traditional fitting methods is impossible. QMC simulations were performed which allow us to model the magnetic behavior from 0.35 to 300 K using three exchange interactions and single-ion anisotropy for nickel. The model predicts weak ferromagnetic exchange interactions, consistent with previous observations^{22,25–27,39–41}, and a spin ground state $S = 91$ and a very large low field magnetic entropy change ($14.1 \text{ J kg}^{-1} \text{ K}^{-1}$ for $\Delta H = 1 \text{ T}$ at 1.1 K).

Methods

Materials and measurements. All reagents and solvents for the syntheses were purchased from commercial sources and used as received. Elemental analyses (C, H, and N) were performed on a Vario EL III elemental analyzer. Infrared spectra ($4000\text{--}400 \text{ cm}^{-1}$) of all samples were recorded on a Thermo Scientific Nicolet 6700 FT-IR spectrophotometer. Magnetic susceptibility measurements were performed on a Quantum Design MPMS-XL7 SQUID magnetometer operating between 2 and 300 K and dc-applied fields ranging from 0 to 7 T. The powder sample was fixed with eicosane and placed in a calibrated gelatine capsule, which was held at the centre of a straw. To prevent the loss of the crystal solvent in **1**, the straw was immediately transferred into the sample chamber of the SQUID at 100 K under helium atmosphere. After the sample space was vent with helium gas and the measurement starts. Background subtractions were performed for the sample holder. Diamagnetic corrections for the sample were applied using with Pascal constants.

Ac susceptibility measurements were extended to the region of very low temperatures by using a home-made micro-SQUID susceptometer⁴². The micro-SQUID has a gradiometric design, with two $30 \mu\text{m}$ wide Nb loops that act as the pick-up coils of the susceptometer. Each of these two loops is placed inside a solenoid that generates the excitation ac magnetic field. The device works in the frequency range 0.01 Hz–250 kHz. It is installed inside the mixing chamber of a $^3\text{He}\text{--}^4\text{He}$ dilution refrigerator, which enables performing experiments between 13 mK and 4.2 K. A grain of powder sample was embedded in grease and placed on top of one of the SQUID loops. The amplitude of the ac magnetic field was 0.05 Oe. Magnetization isotherms were measured between 0.35 K and 5 K with a home-made micro-Hall magnetometer. The sample was placed on the edge of one of the three Hall crosses. A magnetic field $H < 2 \text{ T}$ was applied along the plane of the sensor to minimize its intrinsic bare signal. This signal was calibrated and then subtracted from the results. Heat capacity data were measured, down to $T = 0.35 \text{ K}$, with a commercial physical property measurement system that makes use of the relaxation method⁴³.

Synthesis of $\{\text{Ni}_{21}\text{Gd}_{20}(\text{OH})_{24}(\text{IDA})_{21}(\text{DPGA})_6(\text{C}_2\text{O}_4)_3(\text{NO}_3)_6(\text{CH}_3\text{COO})_3(\text{H}_2\text{O})_{12}\cdot\text{Br}_5\cdot(\text{NO}_3)_4\cdot 30\text{H}_2\text{O}\cdot 20\text{CH}_3\text{OH}$ (1**).** Iminodiacetic acid (0.133 g, 1.0 mmol), diphenylglycolic acid (0.228 g, 1.0 mmol), $\text{Ni}(\text{CH}_3\text{COO})_2\cdot 4\text{H}_2\text{O}$ (0.311 g, 1.25 mmol), $\text{Gd}(\text{NO}_3)_3\cdot 6\text{H}_2\text{O}$ (0.564 g, 1.25 mmol), KBr (0.1 g, 1.7 mmol) and triethylamine (3.0 mmol) were dissolved in mixed solvent of $\text{H}_2\text{O}/\text{CH}_3\text{OH}$ (8 mL, $v/v = 1:1$). This solution was then sealed in a 15 mL Teflon-lined stainless steel vessel and heated at $160 \text{ }^\circ\text{C}$ for 3 days. At a rate of $5 \text{ }^\circ\text{C}/\text{h}$, the system was allowed to cool to room temperature. Green block-shaped crystals of **1** were collected, washed thoroughly with methanol, and dried in air at room temperature (yield ca. 35% on the basis of Ni). Elemental analysis calcd (for $\text{C}_{200}\text{H}_{362}\text{N}_{31}\text{Ni}_{21}\text{Br}_5\text{Gd}_{20}\text{O}_{236}$: C 20.44, H 3.10, N 3.69; Found: C 20.22, H 2.97, N 3.60. Infra-red (KBr disc): $\tilde{\nu} = 3434 \text{ (m)}$, 1573 (s) , 1412 (s) , 1108 (w) , 1020 (m) , 954 (w) , 727 (m) , 670 (m) , 615 (m) .

X-ray structure determination. Single-crystal X-ray diffraction data were collected on a Bruker Apex DUO diffractometer with Mo K α radiation ($\lambda = 0.71073 \text{ \AA}$) at 296 K. The structure was solved by direct methods and all non-H atoms were subjected to anisotropic refinement by full-matrix least-squares refinement on F^2 using SHELXTL. Because of disorder, the two phenyl rings of DPGA²⁻ were both splitted into two parts (C19–C24 and C19A–C24A for one phenyl ring, and C25–C30 and C25A–C30A for another one), which were refined under AFIX 66. There are 20 disordered methanol molecules and 30 disordered water molecules per formula unit that were removed by SQUEEZE in the refinement, but accurately

confirmed by both elemental analyses and charge balance. Refinement parameters and crystallographic data for **1** are shown in Supplementary Table 1.

Data availability. The X-ray crystallographic coordinates for structure reported in this study have been deposited at the Cambridge Crystallographic Data Centre (CCDC), under deposition number 1501498. The data can be obtained free of charge via www.ccdc.cam.ac.uk/data_request/cif. All other data are available from the authors upon reasonable request.

Received: 17 March 2017 Accepted: 4 May 2018

Published online: 29 May 2018

References

- Stamatatos, T. C., Abboud, K. A., Wernsdorfer, W. & Christou, G. “Spin tweaking” of a high-spin molecule: an Mn_{25} single-molecule magnet with an $S = 61/2$ ground state. *Angew. Chem. Int. Ed.* **46**, 884–888 (2007).
- Manoli, M. et al. Magnetic “molecular oligomers” based on decametallate super-tetrahedra: a giant Mn_{49} cuboctahedron and its $\text{Mn}_{25}\text{Na}_4$ fragment. *Angew. Chem. Int. Ed.* **55**, 679–684 (2016).
- Liu, J.-L., Chen, Y.-C., Guo, F.-S. & Tong, M.-L. Recent advances in the design of magnetic molecules for use as cryogenic magnetic coolants. *Coord. Chem. Rev.* **281**, 26–49 (2014).
- Zheng, Y.-Z., Zhou, G.-J., Zheng, Z. & Winpenny, R. E. P. Molecule-based magnetic coolers. *Chem. Soc. Rev.* **43**, 1462–1475 (2014).
- Wang, Y. et al. Mn_{12} single-molecule magnet aggregates as magnetic resonance imaging contrast agents. *Chem. Commun.* **47**, 3541–3543 (2011).
- Pablico-Lansigan, M. H. et al. Magnetic nanobeads as potential contrast agents for magnetic resonance imaging. *ACS Nano*. **7**, 9040–9048 (2013).
- Ako, A. M. et al. A ferromagnetically coupled Mn_{19} aggregate with a record $S = 83/2$ ground spin state. *Angew. Chem. Int. Ed.* **45**, 4926–4928 (2006).
- Kang, S. et al. A ferromagnetically coupled Fe_{42} cyanide-bridged nanocage. *Nat. Commun.* **6**, 5955 (2015).
- Baniodeh, A. et al. High spin cycles: topping the spin record for a single molecule verging on quantum criticality. *NPJ Quantum Mater.* **3**, 10 (2018).
- Tabrizi, S. G., Arbuznikov, A. V. & Kaupp, M. Understanding thermodynamic and spectroscopic properties of tetragonal Mn_{12} single-molecule magnets from combined density functional theory/spin-hamiltonian calculations. *J. Phys. Chem. A* **120**, 6864–6879 (2016).
- Mazurenko, V. V. et al. First-principles modeling of magnetic excitations in Mn_{12} . *Phys. Rev. B* **89**, 214422 (2014).
- Zhang, J., He, L., Cao, H., Wang, F. & Zhang, P. Magnetic exchange couplings in the single-molecule magnet of $\text{Mn}_{12}\text{--Ac}$. *J. Chem. Phys.* **128**, 154711 (2008).
- Engelhardt, L. & Schröder, C. *Molecular Cluster Magnets* 241–291 (World Scientific Publishers, Singapore, 2011).
- Engelhardt, L. P. et al. Octa-, deca-, trideca-, and tetradecanuclear heterometallic cyclic chromium–copper cages. *Angew. Chem. Int. Ed.* **47**, 924–927 (2008).
- Martin, C. et al. Radio-frequency spectroscopy of the low-energy spectrum of the magnetic molecule $\text{Cr}_{12}\text{Cu}_2$. *Phys. Rev. B* **80**, 100407(R) (2009).
- Fang, X. et al. $\{\text{Mo}_{24}\text{Fe}_{12}\}$ macrocycles: anion templation with large polyoxometalate guests. *Angew. Chem. Int. Ed.* **52**, 10500–10504 (2013).
- Qin, L. et al. Quantum Monte Carlo simulations and high-field magnetization studies of antiferromagnetic interactions in a giant hetero-spin ring. *Angew. Chem. Int. Ed.* **56**, 16571–16574 (2017).
- Todea, A. M. et al. Extending the $\{(\text{Mo})\text{Mo}_3\}_{12}\text{M}_{30}$ capsule Keplerate sequence: a $\{\text{Cr}_{30}\}$ cluster of $S = 3/2$ metal centers with a $\{\text{Na}(\text{H}_2\text{O})_{12}\}$ encapsulate. *Angew. Chem. Int. Ed.* **46**, 6106–6110 (2007).
- Evangelisti, M. et al. Cryogenic magnetocaloric effect in a ferromagnetic molecular dimer. *Angew. Chem. Int. Ed.* **50**, 6606–6609 (2011).
- Evangelisti, M. et al. Spin-enhanced magnetocaloric effect in molecular nanomagnets. *Appl. Phys. Lett.* **87**, 072504 (2005).
- Evangelisti, M. et al. Molecular nanoclusters as magnetic refrigerants: the case of Fe_{14} with very large spin ground-state. *Polyhedron* **24**, 2573–2578 (2005).
- Chen, W.-P. et al. A mixed-ligand approach for a gigantic and hollow heterometallic cage $\{\text{Ni}_6\text{RE}_6\}$ for gas separation and magnetic cooling applications. *Angew. Chem. Int. Ed.* **55**, 9375–9379 (2016).
- Peng, J.-B. et al. A 48-metal cluster exhibiting a large magnetocaloric effect. *Angew. Chem. Int. Ed.* **50**, 10649–10652 (2011).
- Zheng, Y.-Z., Evangelisti, M. & Winpenny, R. E. P. Large magnetocaloric effect in a Wells–Dawson type $\{\text{Ni}_6\text{Gd}_6\text{P}_6\}$ cage. *Angew. Chem. Int. Ed.* **50**, 3692–3695 (2011).
- Li, T. et al. Construction of magnet-type coordination polymers using high-spin $\{\text{Ni}_4\}$ -citraete cubane as secondary building units. *Dalton. Trans.* **45**, 10798–10806 (2016).

26. Xiang, S. et al. A fan-shaped polynuclear Gd_6Cu_{12} amino acid cluster: a “hollow” and ferromagnetic $[Gd_6(\mu_3-OH)_8]$ octahedral core encapsulated by six $[Cu_2]$ glycinato blade fragments. *J. Am. Chem. Soc.* **129**, 15144–15146 (2007).
27. Kong, X.-J. et al. Dual shell-like magnetic clusters containing Ni^{II} and Ln^{III} ($Ln = La, Pr, \text{ and } Nd$) ions. *Inorg. Chem.* **47**, 2728–2739 (2008).
28. Bauer, B. et al. The ALPS project release 2.0: open source software for strongly correlated systems. *J. Stat. Mech. Theory Exp.* **2011**, P05001 (2011).
29. Albuquerque, A. F. et al. The ALPS project release 1.3: open-source software for strongly correlated systems. *J. Magn. Magn. Mater.* **310**, 1187–1193 (2007).
30. Liu, D.-P. et al. Magnetic properties of a single-molecule lanthanide –transition-metal compound containing 52 gadolinium and 56 nickel atoms. *Angew. Chem. Int. Ed.* **55**, 4532–4536 (2016).
31. Martínez-Pérez, M. J. et al. Gd-based single-ion magnets with tunable magnetic anisotropy: molecular design of spin qubits. *Phys. Rev. Lett.* **108**, 247213 (2012).
32. Chang, L.-X., Xiong, G., Wang, L., Cheng, P. & Zhao, B. A 24-Gd nanocapsule with a large magnetocaloric effect. *Chem. Commun.* **49**, 1055–1057 (2013).
33. Liu, S.-J. et al. An unprecedented decanuclear Gd^{III} cluster for magnetic refrigeration. *Inorg. Chem.* **52**, 9163–9165 (2013).
34. Pineda, E. M. et al. Molecular amino-phosphonate cobalt–lanthanide clusters. *Chem. Commun.* **49**, 3522–3524 (2013).
35. Peng, J.-B. et al. High-nuclearity 3d-4f clusters as enhanced magnetic coolers and molecular magnets. *J. Am. Chem. Soc.* **134**, 3314–3317 (2012).
36. Zheng, Y. et al. Molybdate templated assembly of $Ln_{12}Mo_4$ -type clusters ($Ln = Sm, Eu, Gd$) containing a truncated tetrahedron core. *Chem. Commun.* **49**, 36–38 (2013).
37. Guo, F.-S. et al. Anion-templated assembly and magnetocaloric properties of a nanoscale $\{Gd_{38}\}$ cage versus a $\{Gd_{48}\}$ barrel. *Chem. Eur. J.* **19**, 14876–14885 (2013).
38. Zheng, Y.-Z., Pineda, E. M., Helliwell, M. & Winpenny, R. E. P. Mn^{II} - Gd^{III} phosphonate cages with a large magnetocaloric effect. *Chem. Eur. J.* **18**, 4161–4165 (2012).
39. Kong, X.-J. et al. A four-shell, 136-metal 3d-4f heterometallic cluster approximating a rectangular parallelepiped. *Chem. Commun.* **0**, 4354–4356 (2009).
40. Zhuang, G.-L., Sun, X.-J., Long, L.-S., Huang, R.-B. & Zheng, L.-S. The synthesis of a 3d–4f polynuclear metal cluster under microwave irradiation: crystal structure and magnetic property of $[La_3Ni_6(IDA)_6(OH)_6(H_2O)_{12}] \cdot 3NO_3 \cdot 15H_2O$ ($IDA = \text{iminodiacetate}$). *Dalton. Trans.* **0**, 4640–4642 (2009).
41. Li, Z.-Y. et al. New 3d–4f heterometallic clusters built from mixed glycine and iminodiacetate acid: dioctahedron $\{La_2Ni_9\}$ and onion-like $\{Gd_5\} \subset \{Ni_{12}\}$ with interesting magnetocaloric effect. *Dalton. Trans.* **42**, 5711–5717 (2013).
42. Bellido, E. et al. Mn_{12} single molecule magnets deposited on μ -SQUID sensors: the role of interphases and structural modifications. *Nanoscale* **5**, 12565–12573 (2013).
43. Evangelisti, M., Luis, F., Jongh, L. J. & Affronte, M. Magnetothermal properties of molecule-based materials. *J. Mater. Chem.* **16**, 2534–2549 (2006).

Acknowledgements

This work was supported by the Natural Science Foundation of China (nos. 21473129, 21620102002, and 21773130), “National Young-1000-Plan” program, State Key Laboratory for Mechanical Behavior of Materials and the Cyrus Chung Ying Tang Foundation.

Author contributions

Y.-Z.Z., L.E., and R.E.P.W. designed and directed the project. W.-P.C. and L.Q. conducted the synthesis and most of the characterization. J.S. and L.E. carried out the detailed quantum Monte Carlo simulations. A.C. and F.L. measured the low-temperature magnetic data. W.-P.C., L.E., F.L., R.E.P.W., and Y.-Z.Z. wrote the manuscript. All authors contributed in important discussions and suggestions on the manuscript.

Additional information

Supplementary Information accompanies this paper at <https://doi.org/10.1038/s41467-018-04547-4>.

Competing interests: The authors declare no competing interests.

Reprints and permission information is available online at <http://npg.nature.com/reprintsandpermissions/>

Publisher's note: Springer Nature remains neutral with regard to jurisdictional claims in published maps and institutional affiliations.



Open Access This article is licensed under a Creative Commons Attribution 4.0 International License, which permits use, sharing, adaptation, distribution and reproduction in any medium or format, as long as you give appropriate credit to the original author(s) and the source, provide a link to the Creative Commons license, and indicate if changes were made. The images or other third party material in this article are included in the article's Creative Commons license, unless indicated otherwise in a credit line to the material. If material is not included in the article's Creative Commons license and your intended use is not permitted by statutory regulation or exceeds the permitted use, you will need to obtain permission directly from the copyright holder. To view a copy of this license, visit <http://creativecommons.org/licenses/by/4.0/>.

© The Author(s) 2018